EXPERIMENTAL CARACTERISATION OF THE RELATIVE GAS PERMEABILITY OF VERY LOW PERMEABILITY ROCKS

F. Bignonnet[1], P. Egermann[2], Z. Duan[3], L.Jeannin[4], F. Skoczylas[3]
1 : Université de Nantes, GeM équipe IEG, UMR CNRS 6183, France
2 : Storengy (ENGIE group), France
3 : Ecole Centrale de Lille, France
4 : ENGIE E&P International, France

This paper was prepared for presentation at the International Symposium of the Society of Core Analysts held in Snowmass, Colorado, USA, 21-26 August 2016

ABSTRACT

The relative gas permeability (k_{rg}) of a low permeability caprock has been measured on a set of samples. The intrinsic gas permeability of the samples are typically in the order of 10^{-4}-10^{-3} mD in the dry state at in-situ confining stress (9 MPa). Water saturations of the samples are achieved by equilibrating them in chambers whose relative humidities are imposed. The measured k_{rg} points lie on a main curve for all the samples and exhibit a very high critical gas saturation (S_{gc}) around 30% above which gas flow can be detected. The origin of this very specific behaviour is discussed using the percolation theory and an analogy with the k_{rg} curves shape observed during depletion tests. A possible explanation involves flow of gas as a discontinuous phase at gas saturations below S_{gc} during the percolation regime, leading to extremely low k_{rg} values with a plateau shape like in depletion tests.

INTRODUCTION

The characterization of low permeability rocks comprising clay is important in the context of unconventional reservoir production, basin modelling and geological storage (CO_2, natural gas,). Nevertheless the available literature data about their associated relative permeabilities are scarce mainly because of the complexity to derive these data in a representative manner and in a reasonable time frame from laboratory experiments (Lefort *et al.*, 2011). This work is a contribution to provide such a dataset in a tight carbonate with a significant clay fraction.

PROCEDURES

Material

The studied material is a caprock, featuring very fine grained carbonate aggregates and minor clay content. All the samples used in this study have been extracted from a core taken from a caprock layer located at a depth around 450 m. A confining pressure of 9 MPa has been assumed representative of in-situ conditions for this layer.

Geochemical analysis indicates that the carbonate content is high with 276,000 parts per million in weight (ppm) of Ca. Additionally, the rock comprises 7,030 ppm of Mg, 7,980 ppm of K, 11,250 ppm of Fe and 6,130 ppm of S, which indicates silicates and clay content. The total organic carbon is 0.57 % and the pyrite component is minor (1.1 %). The anions have not been measured in the "bulk" geochemical analysis, but local EDX analysis indicates that the carbonate is made of tightly packed aggregates of size 1-10 μm, separated by thin layers or canaliculi. The clay content - most likely illite - is located in these thin layers surrounding the carbonate aggregates as well as in isolated high-porosity pockets of micro-metric extension which exhibit micro-metric porosities.

Methods

Sample preparation: Eight vertical cylindrical samples with diameter 37 mm and height 10 mm have been extracted from the main vertical core. The axis of the cylinders is assumed perpendicular to the bedding. The cylindrical samples are first obtained by 37-mm coring, and then cut to the specified length. The faces of the samples are then polished with sandpaper. The height h and diameter d of each sample are then measured with a calliper with a precision of 0.02 mm. The total volume V of each sample is simply assessed by $V = \pi h d^2/4$.

Water Sorption Isotherms and Water Porosity Measurements

Step 1: Drying. All samples are first oven-dried at 60°C until mass stabilisation is achieved, which occurs after about two weeks. This temperature has been chosen to ensure a fairly good state of drying, while limiting the damage (e.g. micro-cracking), which could arise at higher temperatures. This state is considered as the reference dry state, and the water saturation S_w is assumed null. The mass in the dry state m dry is measured with a precision of 0.01g.

Step 2: Water saturation. To obtain a partial water saturation, the samples are stored in a chamber comprising air and water vapour in equilibrium with a saturated saline solution at 20°C (Chen *et al.*, 2012). The relative humidity of the atmosphere in the chamber is imposed by thermo-dynamical equilibrium and depends on the type of saline solution. The relative humidities imposed in the present study range from 43% to 98%.In turn, the capillary pressure $P_{cap} = P_g - P_l$ between the gas (here at atmospheric pressure) and the liquid water (which condenses in the pore network of the sample) is related to the relative humidity RH of the atmosphere by Kelvin's law (first part of equation 1). The capillary pressure is itself related to the curvature of the liquid-gas menisci by Young-Laplace's law (second part of equation 1). If the contact angle between the water and the solid phase is null, the two relations imply:

$$\rho_l RT \ln(1/RH) / M = P_{cap} = 2\gamma / r \qquad (1)$$

where ρ_l is the density of water, M the molar mass of the water, R the perfect gas constant, T the temperature, γ is the coefficient of surface tension, (γ=0.073 N/m for air and water under ambient conditions) and r is a pore size. More precisely, r is either the radius of a cylindrical pore or the distance between the two walls of a flat pore. The capillary pressure thus increases as the relative humidity decreases. For water at 20°C, the

capillary pressures corresponding to the imposed relative humidities range from 2.7 MPa for RH = 98% (corresponding to r=53nm) to 114 MPa for RH = 43% (corresponding to r=1.3nm).

A sample successively equilibrated in chambers with increasing relative humidity undergoes a progressive imbibition, from the smaller to the larger pores. At each step, equilibrium is assumed once mass stabilisation of the sample is achieved, which occurs after about two weeks. The mass m(RH) in the partially water saturated state due to the relative humidity RH is measured with a precision of 0.01 g, and will be used after the third step to deduce the partial water saturation.

Step 3: Total Water Saturation. At the end of the previous steps, the samples are water saturated. To do so, the samples are placed in a vacuumed chamber for 24 hour ; they are partially immersed in water for the 6 first hours to allow the air to drain, then fully immersed. The mass in this saturated state m_{sat} is measured. Assuming the final immersion step guarantees a full water saturation, the porosity φ is:

$$\varphi = (m_{sat} - m_{dry}) / (\rho_l V) \quad (2)$$

Porosity measured using this method will be referred to as "water porosity", as opposed to the "gas porosity" to which it will be compared to later in the paper. Additionally, the partial water saturation $S_w(RH)$ achieved at any of the previous steps by equilibrium with relative humidity RH may now be assessed using

$$S_w(RH) = (m(RH) - m_{dry}) / (m_{sat} - m_{dry}) \quad (3)$$

The $S_w - RH$ curve obtained from equation 3 can be used to derive the capillary pressure curve by means of Kelvin's law (equation 1, left). The latter may be used with caution to estimate the pore size distribution through Young-Laplace's law (equation 1, right), provided the pores are assumed to be either cylindrical or flat and connected in a hierarchy from the smallest to the largest.

Gas Porosity Measurements

An alternative porosity measurement method has been also used using a dedicated method (Chen *et al.*, 2013; Nadah *et al.*, 2013) similar in principle to gas pycnometry. The measurement is performed on a dried sample in a confining cell and relies on the injection of 99% pure Argon in the pore network. The room temperature is set to 20°C. Three volumes have to be distinguished: (1) a reference tank with a calibrated volume V_t of 70 mL, (2) the pore volume $\varphi \times V$ to be measured, (3) the volume V_c of the tubes connecting the reference tank to both sides of the sample. The reference tank is initially at a pressure P_t of 1 MPa which is monitored using a pressure sensor with a precision of 100 Pa, whereas the porosity and the connecting tubes are at atmospheric pressure P_{atm} . The valves between the reference tank and the sample are then opened while the pressure in the reference tank is monitored. Once gas pressure and temperature are equilibrated, application of the law of perfect gases in isothermal conditions links the final pressure P_f to the sample porosity through:

$$P_t V_t + P_{atm} (V_c + \varphi V) = P_f (V_t + V_c + \varphi V) \quad (4)$$

The porosity measurement deduced from equation 4 is referred to as "gas porosity". The volume V_c (≈ 5 mL) is measured based on the same principle using a non-porous steel sample.

Gas Permeability Measurements

Gas permeability K is measured using a uniaxial steady state gas flow apparatus. The apparatus consists of a confining cell which is allowed to reach confining pressures P_c as high as 60 MPa, together with a gas injection device (Dana and Skoczylas, 1999, 2002; Lion *et al.*, 2004, Davy *et al.*, 2007; Chen *et al.*, 2012, 2013; Nadah *et al.*, 2013; Duan *et al.*, 2014). The gas used in the current study is 99% pure Argon with a viscosity of $\mu = 2.2\times10^{-5}$ Pa.s.

The injection pressure P_i at the upstream side is set to values ranging from 0.5 MPa to 1.5 MPa, whereas the back-pressure P_d at the downstream side is equal to the atmospheric pressure. The injection pressure is measured with a pressure sensor with a precision of 0.002 MPa. The drainage flow rate q_d at x = h is measured with a set of flow-meters, the finer of them allowing measurement of flow rates from 0.1 ml/min to 1 ml/min with a precision of 0.01 ml/min.

Combining Darcy's law, mass conservation and the law of perfect gases to Klinkenberg's law (1941) to account for slip flow effects yields the expression for the apparent gas permeability K_{app} as a function of the measured drainage flow rate q_d in the steady state regime:

$$K_{app} = K_{int}(1+b/P_m) = 2\mu h P_d q_d / A(P_i^2 - P_d^2) \text{ with } P_m = (P_i + P_d)/2 \qquad (5)$$

where K_{int} is the intrinsic gas permeability, b is Klinkenberg's coefficient and $A = \pi d^2/4$ is the area of the sample section. The equation 5 has been rigorously derived accounting for the non-uniformity of the pressure gradient profile along the sample due to the gas compressibility and is valid irrespective of P_i and P_d, which may be very different. Hence, the plot of K_{app} with respect to $1/P_m$ allows determination of the intrinsic gas permeability and the Klinkenberg coefficient. In practice, three different gas injection pressures are successively applied: 0.5, 1 and 1.5 Mpa.

In order to assess the relative gas permeability as a function of the water saturation S_w, effective gas permeability measurements are performed at each step of saturation obtained by the procedure described above. As the Argon gas injected in the partially water saturated sample is dry, the mass of the sample is checked before and after the measurement to monitor potential desaturation of the sample. In practice for the current study, changes in water saturation due to dry gas injection have been observed to be negligible.

RESULTS

Porosity

The measured "water porosities" (equation 2) and "gas porosities" (equation 4) are reported in Table 1. Water porosities are measured without confining pressure, whereas

gas porosities are measured at three steps of a confining pressure cycle (from 2 MPa to 9 MPa (≈ in-situ pressure) and back to 2 MPa).

	confining pressure (MPa)									
	0	2 → 9 → 2			2	9	2	9	2	9
	porosity				permeability					
sample	water	gas (Argon)			K^{app} (μD) for Pi = 1MPa		K^{int} (μD)		b (MPa)	
MIL-12	10.6	-	-	-	1.44	1.28	0.28	0.23	2.4	2.8
MIL-11	9.6	11.84	10.67	11.53	1.20	1.12	0.18	0.16	3.4	3.6
MIL-14	8.9	12.43	11.69	12.15	1.21	1.13	0.19	0.18	3.3	3.2
MIL-20	14.5	-	-	-	9.41	3.94	7.0	2.4	0.23	0.40
MIL-21	13.3	-	-	-	2.15	1.83	0.55	0.44	1.7	1.9
MIL-22	10.2	12.70	11.79	12.50	1.36	1.26	0.42	0.38	1.1	1.0
MIL-23	9.0	11.65	10.81	11.51	1.13	1.05	0.18	0.16	3.3	3.3
MIL-24	9.1	11.75	11.13	11.77	1.16	1.09	0.19	0.21	3.0	2.5

Table 1. Measured porosities and dry-state gas permeabilities.

Gas porosities exhibit a low dispersion and range from 11.7 to 12.7% at 2 MPa of confining pressure. Water porosities are more dispersed, mostly because of the presence of the two specimens MIL-20 and MIL-21, which have been sampled closer to the upper part of the received core than all other samples.

The water porosities appear to systematically underestimate the gas porosities by 1 to 2 porosity units. As water molecule and Argon atom diameters are respectively 0.28 nm and 0.38 nm, their size cannot explain this discrepancy. The possible origin of this difference may be the sorption of Argon on pore walls during the porosity measurement experiment, which has not been quantitatively assessed.

The confining pressure increase from 2 MPa to 9 MPa leads to a decrease of 1 porosity unit. After unloading, the initial porosity values are retrieved up to the measurement errors. This indicates that the evolution of the samples along the imposed stress path is mostly elastic.

Water Sorption Isotherm, Capillary Curve and Pore Size Distribution

In order to determine the length scales associated with the porosity, the water sorption and desorption curves are measured based on the partial water saturation method described in the previous section. Note that the S_w–RH curves obtained from equation 3

Figure 1. Water sorption-desorption isotherms (left) and inferred cumulative pore size distribution from Kelvin-Laplace's law (right).

and presented in Figure 1 can be used to derive capillary pressure curves by means of Kelvin's law (equation 1).

The desorption curve, which has been measured on a single sample, is slightly above the sorption curves. As for the set of eight sorption curves, the dispersion increases with decreasing capillary pressure ($S_w = 0.68 \pm 0.10$ at $P_{cap} = 2.7$ MPa ; $S_w = 0.115 \pm 0.015$ at $P_{cap} = 114$ MPa). Again, the two specimens MIL-20 and MIL-21, which have the highest total porosities, have also the weakest water saturation at $P_{cap} = 2.7$ MPa. This indicates that the extra porosity of these two specimens is mostly a macro-porosity.

The sorption-desorption curves presented in Figure 1 are re-interpreted as cumulative pore size distributions using Young-Laplace's law (equation 1). To do so, the pores have been assumed flat, i.e. described as the space between two parallel planes with an aperture r, which is of course a rough approximation. Under these assumptions, around 70±5% of the porosity corresponds to pores with an aperture below 50 nm. This fine porosity is attributed to the clay phase, which is located either in the canaliculi spanning carbonate aggregates or in high-porosity pockets. The pore size distribution above 50 nm cannot be evaluated by the present method, but mainly corresponds to the inter-particular pores observed by SEM in the high-porosity pockets.

Gas Permeability

Dry case

The gas permeability has been initially measured on the dried samples using the steady state method. Each sample undergoes a confining pressure cycle from 2 MPa to 9 MPa and back to 2 MPa. At each confining pressure step, the apparent gas permeability is measured for three different gas injection pressures: 0.5 MPa, 1 MPa and 1.5 MPa. Except for the two samples MIL-20 and MIL-21, the apparent gas permeability for an injection pressure of 1 MPa is 1.25±0.15 μD and Klinkenberg corrected intrinsic permeability is 0.24±0.1 μD (see Table 1). The specimens MIL-20 and MIL-21, which

also have more micro-cracks and macro-porosity, have permeabilities 2 to 8 times greater than all other samples.

The moderate increase in confining pressure from 2 to 9 MPa results in a decrease in permeability of only 10%. After unloading to 2 MPa, the initial permeability is almost recovered with less than 5% relative difference. These relatively low fluctuations indicate that the deformation of the samples is mostly elastic during the present load cycle.

Relative gas permeability k_{rg}

In order to assess the relative gas permeability, effective gas permeability measurements are carried out on the partially water saturated samples. At each imposed relative humidity step, the samples undergo the same confining pressure/gas injection pressure cycles as in the dry case.

The measured gas relative permeabilities are reported as a function of water saturation in Figure 2, for confining pressures of 2 and 9 MPa.

Figure 2. Gas relative permeability k_{rg}.

For water saturations below 0.5, effective gas permeabilities exhibited limited hysteresis to a cycle in confining pressure (2→9→2 MPa). However at the highest water saturation tested (corresponding to RH = 98%), the effective gas permeability after the confining pressure cycle ranged only from 1/2 to 1/3 of the value before the cycle, for the same reference value (2 MPa) of confining pressure. Two hypotheses may be proposed to explain this hysteresis: (1) pore compression due to hydrostatic loading induces a spatial reorganisation of the water or (2) the saturation cycle has induced micro-cracking of the samples. Subsequent permeability measurements after a second drying of the samples suggest that limited micro-cracking might indeed have occurred.

Except for the two outlier specimens MIL-20 and MIL-21 which suffered from severe micro-cracking induced by the saturation process, all the measured relative permeabilities in Figure 2 lie on a master curve, for both confining pressures (2 and 9 MPa). The main feature of the relative permeability curve is the presence of a high critical gas saturation S_{gc} around 0.29 ± 0.04 for which gas permeability nearly vanishes. The influence of the

saturation history on the relative permeability curve has not been assessed and requires further investigation. This effect has been studied on two industrial concretes (Chen *et al.*, 2012), evidencing that the saturation history influences k_{rg} mainly in the case of a strong hysteresis in desorption/re-saturation isotherms (i.e. S_w − RH relations), which is not the case of the material presently under consideration (Figure 1).

DISCUSSION

Are the k_{rg} curves obtained relevant for drainage or imbibition ? A priori the saturation protocol relies on a progressive imbibition through the relative humidity technique. Nevertheless, the trapped gas phase is compressed from 1 atm (initial pressure) to very large pressures (Young Laplace) since the pressure is imposed by the size of the throat which trapped the gas. For 50 nm, it gives a pressure of around 30 bars leading to a strong compression and a dissolution of the gas phase in the surrounding water phase. It makes this protocol be an equivalent drainage process since all the gas trapping is progressively and naturally removed by this compression-dissolution mechanism.

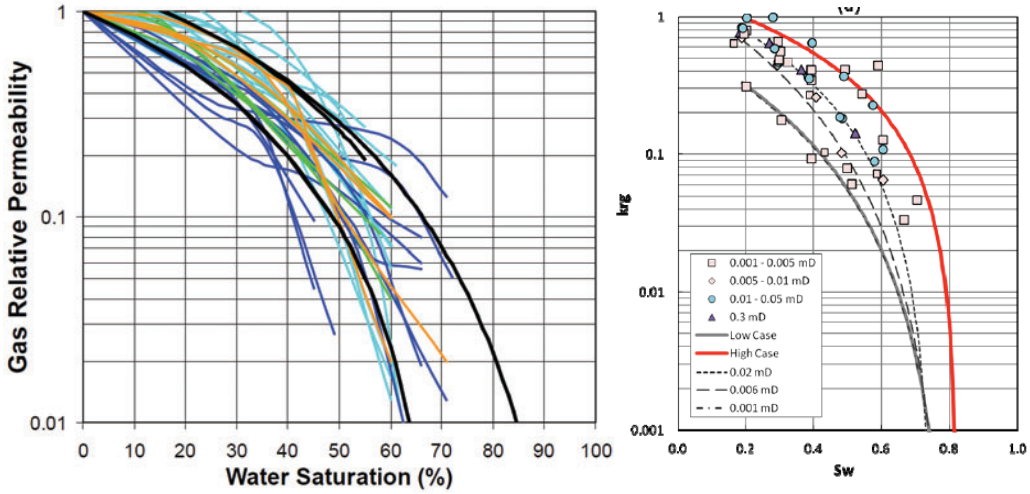

Figure 3. Examples of gas drainage relative permeability curves obtained on tight reservoirs, Cluff and Byrnes, (2010) on the left and Wang et al (2011) on the right)

The gas drainage relative permeability obtained on a caprock facies of extremely low permeability, appear very similar to the ones already published for tight gas reservoirs since they exhibit also very high S_{gc} values (typically in the 15-40% range) as shown in Figure 3 (Cluff and Byrnes,2010; Wang *et al.*, 2011 and Duan *et al.*, 2014). The S_{gc} is defined here as the saturation which corresponds to the apparent beginning of a gas flow in a connected form. Cluff and Byrnes (2010) proposed an empirical formula based on tight reservoir sample to obtain the apparent S_{gc} value ($S_{gc} = 0.15 – 0.05*\log_{10}K$). This does not seem to be applicable for our lower permeability samples since it would give more than 40% rather the observed values in the 25-30% range.

Above the S_{gc} value, the flow topology (connected gas phase) is consistent with the Darcy formalism and therefore a Corey type function appears adequate to reproduce the

general shape of the data (Figure 5). Surprisingly, the gas relative permeability behaviour below S_{gc} has raised little interest to date (Lefort *et al.*, 2011). It is often considered that the gas phase exhibits no mobility at all in this saturation range, which is often referred as the "permeability jail". As pointed out by Cluff and Byrnes (2010), this is not true in a drainage mode by flooding since the gas must have some mobility to make its own saturation increase up to S_{gc}. The expected shape of the k_{rg} curve in this saturation interval have been inferred by combining several sources of information:

1. Although this parameter is difficult to measure directly, both Busch and Amann-Hildenbrand (2013) and Haoguang *et al.* (2014) have reported that very low permeability rocks are characterized by large aspect ratios (pore body size divided by pore throat size). On the opposite, the length ratio (pore body length divided throat length) is small in this particular rocks (elongated throats).

2. Several interesting results can be obtained from the works on the percolation-invasion mechanisms (Lenormand *et al.*, 1983; Wilkinson, 1986). In the percolation regime at low saturation, the k_{rg} is proportional to Sg^{α}. α is in the order of 5 and depends on the conductivity exponent of the medium. It is also established that the aspect ratio plays a major role in the snap-off frequency during the percolation. It therefore suggests that the texture of low permeability rocks significantly favours this mechanism. This could induce the formation of disconnected gas ganglia and a dispersed flow topology at a certain level of gas saturation. This mechanism could be potentially exacerbated by the small length ratio which also prevails in very low permeability rocks. In the configuration of a drainage at low rate with a low viscosity gas phase, the DLA (Diffusion Limited Aggregation) percolation mode is the one which prevails (Lenormand *et al.*, 1988). These snap-off events could occur not only at the flood front but all along the DLA flow path leading to a dispersed, disconnected gas distribution pattern and a reduced gas mobility comparing to what predicts the percolation theory.

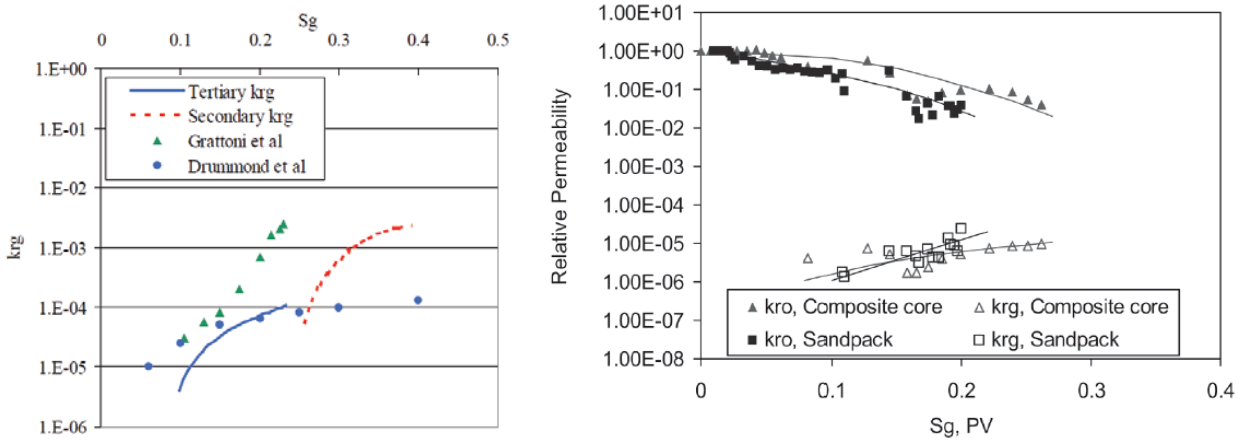

Figure 4. Examples of solution gas relative permeability curves obtained with light oils (Egermann et al., 2004) and heavy oils (Tang et al., 2006)

3. The dispersed flow characteristics have been extensively studied in the context of the recovery processes based on solution gas drive by depletion under secondary / tertiary conditions for both light / heavy oils (Egermann *et al.*, 2004, Bauget *et al.*, 2005, Tang *et al.*, 2006). In these cases, the discontinuous gas phase is created in-situ by nucleation and then diffusion from the solution gas. The DLA – snap-off events suspected in low permeability rocks could conduct to a similar gas distribution pattern once the gas saturation reached a certain value. All the results from the studies on solution gas drive mechanisms converge towards a very typical shape of the k_{rg} curves with a plateau at very low values (Figure 4). Whatever the type of fluid system considered, the plateau is typically located below 10^{-3}-10^{-4}.

By combining these various sources of information, it is then possible to propose what the global k_{rg} shape could be over the whole saturation range. At low saturation (Figure 5 left red curves), the percolation k_{rg} curve is quite steep rather the solution gas drive like k_{rg} curve exhibits a plateau ending at around 10^{-4}. This value is completely speculative and has been chosen only because it seems representative of the values found for similar viscosity ratio cases. Additional studies would be needed to better assess this value according to the rock and fluid/system. At very low S_g, the percolation k_{rg} curve is more relevant (see paragraph 3 above). At higher S_g, a dispersed gas flow regime could start before S_{gc} and then the connected flow (blue part). The proposed shape of k_{rg} below the apparent S_{gc} is a composite curve built from percolation and dispersed flow theory (Figure 5 right green curve). It is interesting to notice that this composite curve is normally completely hidden because the measurement of such low values of k_{rg} are not accessible with standard protocols with low permeability rocks.

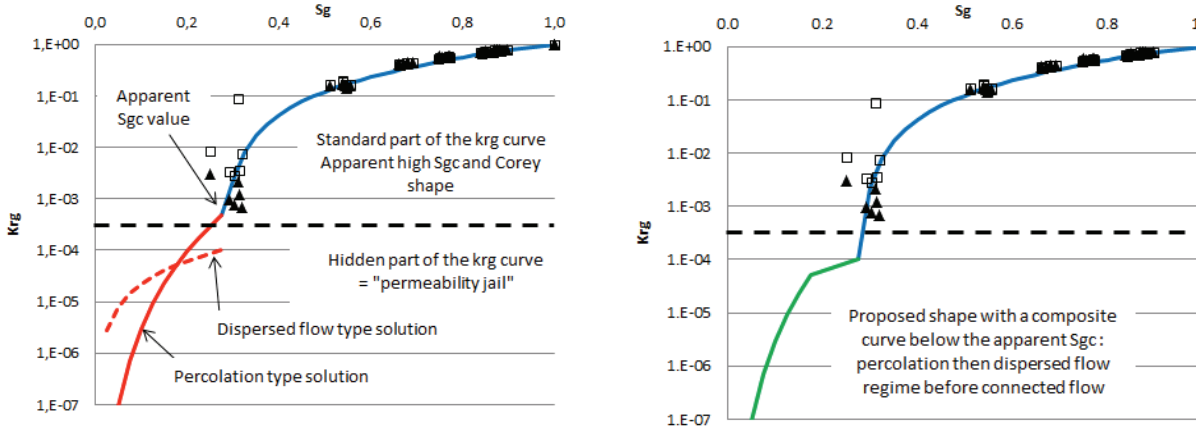

Figure 5. Possible shape of the global krg curve over the whole saturation range for very low K rocks

Having the complete shape of the k_{rg} is of interest for various industrial applications especially those with large time scales, which give more importance about the role played by low k_{rg} values. It concerns mainly the applications related to the basin modelling simulation; the CO_2 storage or the nuclear waste storage (evolution of the associated H_2 produced) where accurate and complete k_{rg} curve description is needed to assess the long fate of the gas phase.

The specific k_{rg} curve shape has also strong implications for gas storage applications since it implies that the gas mobility is very limited at low saturation. It means that a caprock exhibits two interesting features in term of confinement properties. The first is the standard one which consists in a static barrier related to the threshold capillary pressure value. The second one, evidenced by this work, consists in a dynamic barrier, related to the specific gas relative permeability curve shape, which delays significantly the gas flow at low saturations.

CONCLUSION

This paper provides a new complete set of experimental data at various confining pressures to characterize a caprock facies including porosity accessible to gas or water, water sorption-desorption isotherms and gas permeabilities as a function of water saturation, gas injection pressure and confining pressure. The measured relative gas permeabilities lie on a main curve for all samples and exhibit a very high critical gas saturation around 30% where gas flow can be detected. This behaviour is very specific and was already evidenced on tight reservoir samples. Several pieces of information about the pore texture in low permeability rocks, the percolation-invasion mechanisms and the works conducted for determining flow parameters under solution gas drive, have been combined to assess the flow behaviour below this apparent S_{gc} value. A composite curve is proposed which exhibits extremely low gas relative permeability far below the limit of what can be measured in the laboratory in such rocks. When the gas saturation becomes large enough, a connected flow can take place and be measured. This specific behaviour consists in a key feature for various industrial applications with large characteristic times since it rules the flow kinetic in this low gas saturation range and k_{rg} values.

ACKNOWLEDGEMENTS

We are grateful to ENGIE E&P International and Storengy (ENGIE group) for permission to publish these results and to R. Lenormand for fruitful discussions.

REFERENCES

F. Bauget, P. Egermann, R. Lenormand, “A new model to obtain representative field relative permeability for reservoirs produced under solution gas drive”, *SPEREE*, (August 2005), 348-356.

A. Busch, A. Amann-Hildenbrand, “Predicting capillarity of mudrocks”, *Marine and Petroleum Geology,* (2013) **45**, 208-223.

W. Chen, J. Liu, F. Brue, F. Skoczylas, C.A. Davy, X. Bourbon, and J. Talandier, “Water retention and gas relative permeability of two industrial concretes,” *Cement and Concrete Research*, (2012) **42,** 1001–1013.

X.T. Chen, G. Caratini, C.A. Davy, D. Troadec, and F. Skoczylas, “Coupled transport and poro-mechanical properties of a heat-treated mortar under confinement”, *Cement and Concrete Research*, (2013) **49,** 10–20.

R.M. Cluff, A.P. Byrnes, “Relative permeability in tight gas sandstone reservoirs – The “permeability jail” model”, *SPWLA 51th Annual Logging Symposium*, (June 19-23, 2010).

E. Dana and F. Skoczylas, “Gas relative permeability and pore structure of sandstones”, *International Journal of Rock Mechanics and Mining Sciences*, (1999) **36**, 613–625.

E. Dana and F. Skoczylas, “Experimental study of two-phase flow in three sandstones. I. Measuring relative permeabilities during two-phase steady-state experiments”, *International Journal of Multiphase Flow*, (2002) **28,** 1719–1736.

C.A. Davy, F. Skoczylas, J.D. Barnichon, and P. Lebon, “Permeability of macro-cracked argillite under confinement: Gas and water testing”, *Physics and Chemistry of the Earth*, (2007) **32**, 667–680.

Z. Duan, C.A. Davy, F. Agostini, L. Jeannin, D. Troadec, and F. Skoczylas, “Gas recovery potential of sandstones from tight gas reservoirs”, *International Journal of Rock Mechanics & Mining Sciences*, (2014) **65**, 75–85.

P. Egermann, S. Banini, O. Vizika, “Depressurization under tertiary conditions in the near-wellbore region: experiments, visualization and radial flow simulations”, *Petrophysics*, (Sept-October 2004) **45**, n°5.

W. Haoguang, M. Kun, Y. Xiang’an, W. Xinxin, “The relationship of ultra-low permeability sandstone aspect ratio with porosity, permeability”, *Advances in Petroleum Exploration and Development*, (2014) **7**, n°1, 7-12.

L. J. Klinkenberg, “The permeability of porous media to liquids and gases”, In *API Drilling and Production Practices*, New York, API 11th mid-year meeting, Tulsa (1941), 200–213.

R. Lenormand, C. Zarcone, A. Sarr, “Mechanisms of the displacement of one fluid by another in a network of capillary ducts”, *J. Fluid Mech.*, (1983) **135**, 337-353.

R. Lenormand, E. Touboul, and C. Zarcone, “Numerical models and experiments on immiscible displacements in porous media”, *J. Fluid Mech.*, (1988) **189**, 165-187.

M. Lion, F. Skoczylas, and B. Ledésert, “Determination of the main hydraulic and poro-elastic properties of a limestone from Bourgogne, France”, *International Journal of Rock Mechanics & Mining Sciences*, (2004) **41**, 915–925.

J. Nadah, F. Bignonnet, C. A. Davy, F. Skoczylas, D. Troadec, and S. Bakowski, “Microstructure and poro-mechanical performance of Haubourdin chalk”, *International Journal of Rock Mechanics & Mining Sciences*, (2013) **58**, 149–165.

G.-Q. Tang, A. Sahni, F. Gadelle, M. Kumar, A.R. Kovscek, 'Heavy-oil solution drive in consolidated and unconsolidated rock”, *SPE Journal*, (June 2006), 259-268.

D. Wilkinson, “Percolation effects in immiscible displacement”, *Physical review A*, (1986) **34**, n°2, 1380-1391.

P. Lefort, V. Sarrot, M. Prat, J. Talandier, “Hyperslow drainage”, *20ème congrès français de mécanique*, 29 août-2 septembre 2011, Besançon, France.

Y. Wang, Z. Chen, V. Morah, R. J. Knabe and M. Appel. *Gas phase relative permeability characterization on tight gas samples.* SCA2011-13.